Nano Research

Open Access

Research Article

Large-sized nanostructure electrodes for anion exchange membrane water electrolysis

Hang Lei[1] ✉, Yifan Zhou[1], Qixiang Wan[2], Meng-Qiu Chen[2], Xuelin Yang[1], Xi-Bo Li[2] ✉, Zilong Wang[2] ✉, Wenjie Mai[2], and Shichun Mu[3] ✉

[1] *Hubei Provincial Collaborative Innovation Center for New Energy Microgrid, College of Electrical Engineering & New Energy, China Three Gorges University, Yichang 443002, China*

[2] *Siyuan Laboratory, Guangdong Provincial Engineering Technology Research Center of Vacuum Coating Technologies and New Energy Materials, Guangdong Provincial Key Laboratory of Nanophotonic Manipulation, Department of Physics, College of Physics and Optoelectronic Engineering, Jinan University, Guangzhou 510632, China*

[3] *State Key Laboratory of Advanced Technology for Materials Synthesis and Processing, Wuhan University of Technology, Wuhan 430070, China*

Cite this article: *Nano Research*, **2026**, *19*, 94908557. https://doi.org/10.26599/NR.2026.94908557

ABSTRACT: One of challenges for industrial water electrolysis is to achieve large-sized electrodes with high structural uniformity and reaction stability. Here, catalyst electrodes of water electrolyzer with delicate nanostructures are fabricated through a facile corrosion engineering and ion regulation co-strategy. Herein the corrosion engineering is an energy efficient (60 °C, 10 min) and scalable route to transforming the commercial nickel foam into catalytic active materials, while the introduction of suitable anions in solutions induces the formation of ordered vanadium (V)-doped RuNi nanoparticles (denoted as V-RuNi) and tungsten (W)-doped NiFe nanowire arrays (denoted as W-NiFe) available to catalyze hydrogen/oxygen evolution reactions. The ion doping effect is proposed to explain the enhanced catalytic activity. Then an anion exchange membrane (AEM) water electrolyzer (electrode area: 19 cm × 19 cm) is assembled and operates stably for 200 h at a high current of 10 A with negligible degradation. This work provides a research paradigm to realize the large-area fabrication of low-cost catalyst electrodes for industrial hydrogen generation via water electrolysis.

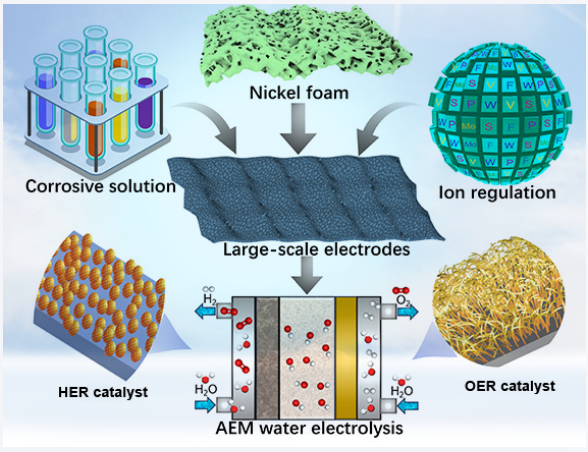

KEYWORDS: electrocatalysts, corrosion engineering, large-scale electrodes, water splitting, hydrogen energy

1 Introduction

Hydrogen energy has been regarded as one of the main paths for the transformation of global traditional fossil fuels to sustainable energy [1, 2]. Electrocatalytic water splitting can produce high-purity hydrogen with much-reduced carbon emission, which is an ideal technology to produce hydrogen for sustainable energy [3, 4].

Received: January 21, 2026; **Revised:** February 8, 2026
Accepted: February 10, 2026

✉Address correspondence to Hang Lei, leihang@ctgu.edu.cn; Xi-Bo Li, lixibo@jnu.edu.cn; Zilong Wang, zilong@email.jnu.edu.cn; Shichun Mu, msc@whut.edu.cn

For an electrolysis cell, both the cathodic hydrogen evolution reaction (HER) and anodic oxygen evolution reaction (OER) require efficient catalysts to reduce the potential required to drive the water splitting reactions [5, 6]. This has stimulated extensive research efforts to develop low-cost electrocatalysts. Recently, various non-precious metal-based electrocatalysts (e.g., metal compounds and their hybrids) have been explored to replace noble metals (e.g., Pt/C, IrO_2, and RuO_2) for water electrolysis [7–10]. While some of these catalysts have demonstrated exceptional catalytic activity and stability beyond that of precious metal catalysts under laboratory conditions, there are still major obstructions to employing them for industry applications [11–13]. The main challenge is high production cost, tedious and multistep synthetic procedure that may require high temperatures or electricity input, and even the consumption of high-purity gas (e.g., H_2, N_2, and

NH_3) [14]. Hence, most laboratory-scale preparation methodologies are not economical for large-scale applications in industry [15–17]. Another consideration is that the release of generated bubbles and long-term durability at high currents (hundreds of $mA{\cdot}cm^{-2}$) are closely related to the microstructure of the electrodes, for which well-defined and robust nanostructures are preferred [18, 19]. However, rapid synthesis of large-sized catalyst electrodes with well-designed nanostructures has been rarely reported.

The corrosive metal substrates (e.g., Ni/Fe foam) possess abundant active substances (metal (oxy)hydroxide/oxide). A top-down synthesis approach by etching metal substrates may provide an efficient and cost-effective route to the preparation of self-supported catalyst electrodes [20]. However, metal (oxy)hydroxide/oxide formed by natural corrosion has poor catalytic activity, and the free-standing electrode surface usually shows a random microstructure. The dynamic corrosion behaviors are closely related to the corrosive environments, and the corrosion process will be accelerated in the presence of various ions in humid environments [21]. Furthermore, different ions introduced in the corrosion process can effectively optimize the electronic structure, morphology, conductivity, and hydrophilicity of host materials [22–24]. This renders flexibility in tuning the catalytic function. Especially, the rational corrosion engineering and ion regulation will benefit the long-term stability of the electrocatalyst. Hence, combining corrosion engineering with ion regulation could be a highly feasible strategy to fabricate low-cost catalysts for water splitting reactions. Nevertheless, few studies are available to implement this strategy for preparing catalysts on a large-scale and to bridge the gap between laboratory advances and industrial expectations in water electrolysis.

Herein, we construct large-sized HER and OER electrodes with uniform nanostructures through a corrosion engineering and ion regulation strategy as an energy efficient (60 °C) and time-saving (10 min) route. The etching of commercial Ni foam (NF) is facilitated by adding different ions into the corrosion solution. The one-step method rapidly transforms the surface of NF into uniform vanadium (V)-doped RuNi nanoparticles (denoted as V-RuNi) and vertical tungsten (W)-doped NiFe nanowire arrays (denoted as W-NiFe), both exhibiting spatially uniform nanostructures and superaerophobic features. For this fabrication approach, the size of electrodes is limited only by the synthesis apparatus. As a case study, we perform the obtained V-RuNi and W-NiFe electrode for HER and OER, respectively. The anion exchange membrane (AEM) electrolyzer, with V-RuNi and W-NiFe catalyst layers (both 19 cm × 19 cm) at anode and cathode, respectively, achieves a low cell voltage of 2.32 V at a current of 5 A for overall water splitting and maintains 200 h durability at the current of 10 A. Undoubtedly, such a simultaneous synthesis of large-sized HER and OER electrodes with uniform nanostructures will benefit the hydrogen energy industry and carbon-neutral targets.

2 Results and discussion

The HER and OER catalyst electrodes were synthesized by combining corrosive engineering with ion regulation on the NF substrate in aqueous solutions (Fig. 1(a)). HER catalysts were obtained by immersing bare NF in a solution containing $RuCl_3$ and different kinds of sodium salts (VO_4^{3-}, MoO_4^{2-}, WO_4^{2-}, S^{2-}, $H_2PO_4^-$, $H_2PO_2^-$, and F^-) and kept at 60 °C for 10 min. Ru^{3+} was chosen to react with NF mainly because Ru-based nanomaterials exhibit remarkable adsorption of hydrogen-containing intermediates [25]. The addition of different ions can effectively modulate the corrosive environment, thus regulating the corrosion rate of Ru^{3+} on Ni metal and the surface morphology of the electrodes [26–28]. The NF not only acts as a conductive support but also as an inexpensive Ni source. Linear scanning voltammetry (LSV) measurements demonstrate optimal catalytic activity upon VO_4^{3-} introduction (Fig. 1(b) and Fig. S1(a) in the Electronic Supplementary Material (ESM)); this electrode is designated as V-RuNi. The synthesis path of the OER catalysts was basically the same as that of HER one, except that Fe^{3+} reacts with NF, and the detailed method can be found in Experimental section in the ESM. Similarly, the best OER catalyst electrode (W-NiFe) was obtained from the introduction of sodium tungstate (Fig. 1(b) and Fig. S1(b) in the ESM). As a result, we chose V-RuNi and W-NiFe as the samples for further investigation.

To explore the effect of the V/W introduction on the properties of the electrocatalysts, the surface morphology and chemical composition of as-prepared electrocatalysts were fully characterized. For the original RuNi electrode for HER without V introduction, the scanning electron microscopy (SEM) images show the catalytic active layer is not densely packed with the inner Ni metal (Fig. 1(c)) and present uneven cracks (Figs. S2(a) and S2(b) in the ESM), leading to easy peeling of the catalytic active layer from the Ni substrate during the HER process at high current densities. This is detrimental to the long-term stability of this electrode. A closer inspection of the surface reveals that the active layer consists of homogeneous nanoparticles (Fig. S2(c) in the ESM). In comparison, the active layer of the V-RuNi electrode is very dense after the introduction of V, and does not tend to peel off from the internal Ni substrate (Fig. 1(d)). Furthermore, the catalytically active layer has been etched into tiny parts separated by small cracks (Figs. S3(a) and S3(b) in the ESM). This V-RuNi electrode surface also exhibits a morphology of uniform nanoparticles (insert in Fig. 1(d)), which are densely dispersed on the Ni substrate. Furthermore, the high-angle annular dark-field scanning transmission electron microscopy (HAADF-STEM) image shows the uniform dispersion of V-RuNi nanoparticles, and the corresponding elemental mapping images show the homogeneous distribution of V, Ru, Ni, and O elements, which also confirms that V has been introduced into RuNi (Figs. 1(e) and 1(f)).

Similarly, there are also major differences in the nanostructures of the initial NiFe catalysts from the W-NiFe. As shown in Fig. 1(g) and Fig. S4 in the ESM, the surface of the original NiFe electrode is extremely rough and shows irregular nanostructures, together with some irregularly shaped large particles. After the incorporation of W, the W-NiFe electrode is covered by a dense array of vertical nanowires (Fig. 1(h)). The nanowires interlocked with each other to form a bird nest-like clump (Fig. S5 in the ESM). Furthermore, the morphology of nanowires and composition of W-NiFe are proven by HAADF-STEM image and the elemental mapping images (Figs. 1(i) and 1(j)). The morphology of NiFe-based catalysts incorporating other types of sodium salts (Na_2MoO_4, Na_2S, NaH_2PO_4, NaH_2PO_2, and NaF) was also explored. As depicted in Fig. S6 in the ESM, the NiFe-based catalysts exhibit distinct morphological variations after incorporating various sodium salts, underscoring the impact of ion regulation on the catalyst microstructure. Only the addition of sodium tungstate induces the formation of a nanowire array structure. During the corrosion process, anions (MoO_4^{2-}, S^{2-}, $H_2PO_4^-$, $H_2PO_2^-$, and F^-) regulate

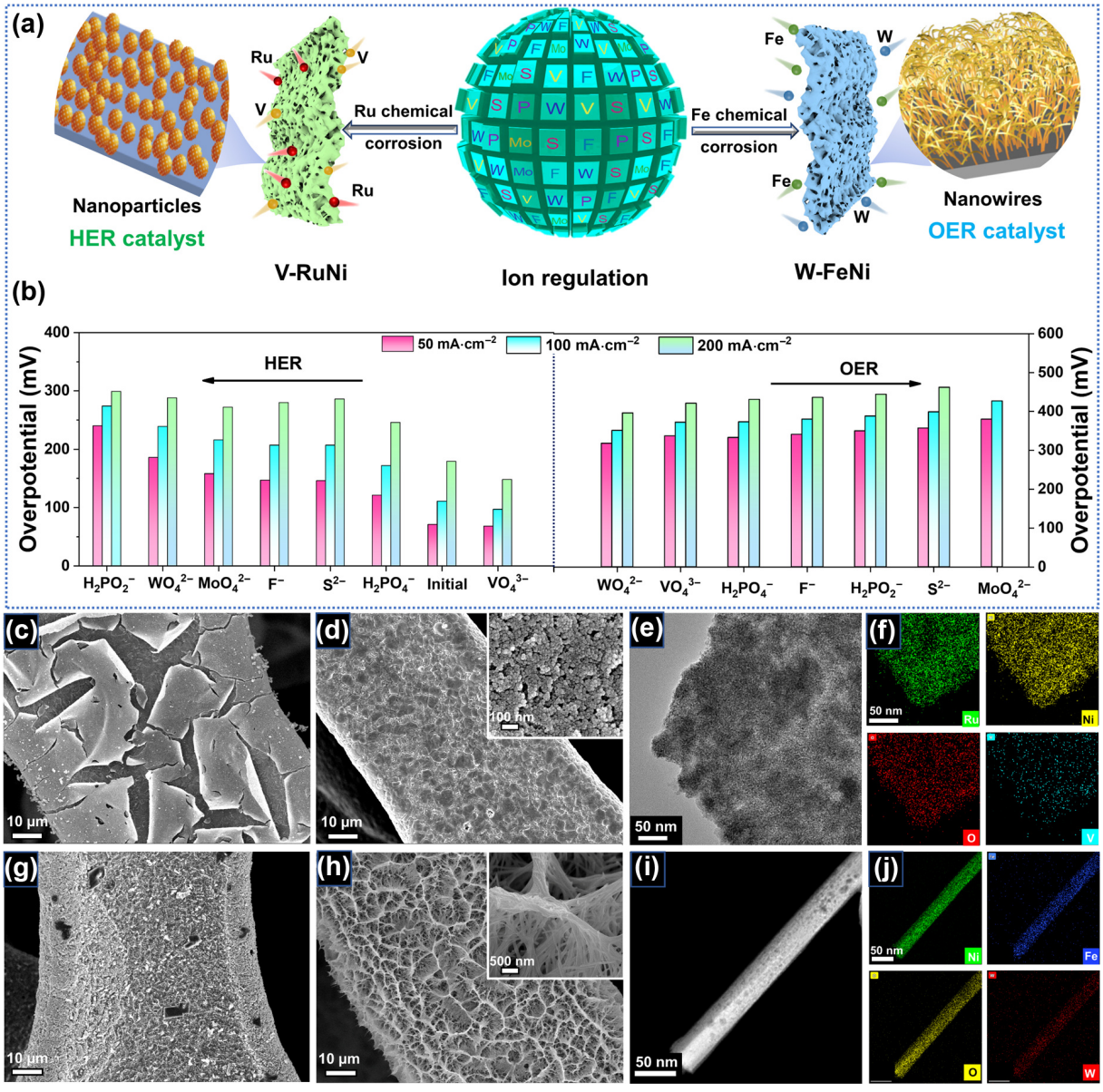

Figure 1 Synthetic pathways, catalytic performance, and micromorphological characterization of various catalysts. (a) Schematic illustration of corrosion engineering and ion regulation for the synthesis of OER and HER catalysts. The sphere in the middle indicates that various elements can be used for the corrosion solution. (b) Overpotentials of catalyst electrodes were obtained by introducing different kinds of ions (sodium salts) at three high current densities. SEM images of (c) RuNi and (d) V-RuNi at different resolutions. (e) HAADF-STEM image and (f) the corresponding elemental mapping images of Ru, Ni, O, and V. SEM images of (g) NiFe and (h) W-NiFe at different resolutions. (i) HAADF-STEM image and (j) the corresponding elemental mapping images of Ni, Fe, O, and W.

corrosion/redeposition kinetics, thereby controlling the density and morphology of the corrosion layer.

The X-ray diffraction (XRD) patterns (Fig. S7 in the ESM) of V-RuNi and W-NiFe show the absence of characteristic diffraction peaks except for the Ni substrate, indicating their low crystallinity or amorphous features. The Raman results show that both V-RuNi and W-NiFe are hydroxide phases (Fig. S8 in the ESM). In Fig. S9 in the ESM, after the introduction of V, both Ru 3p and Ni 2p X-ray photoelectron spectroscopy (XPS) spectra of V-RuNi positively shift, suggesting the changes in the internal electronic structure and metal coordination environment [29–31]. Similarly, both $2p_{1/2}$ and $2p_{3/2}$ in the Ni 2p spectra of W-NiFe positively shift after W integration (Fig. S10(a) in the ESM), which indicates the increase of oxidation state of Ni. However, the Fe 2p binding energies are unchanged (Fig. S10(b) in the ESM), indicating the stable valence state of Fe species [32]. According to XPS spectra, the atomic ratios of V and W in V-RuNi and W-FeNi are 0.5% and 0.27%, respectively. The above characterization suggests that the introduction of V/W not only regulates the surface nanostructure but also the electronic structure of the electrocatalysts.

The surface corrosion engineering and ion regulation strategy efficiently transforms the smooth surface of commercial Ni foam into catalytically active layers with well-defined nanostructures. This cost-effective and time-saving method, which requires no electrical input, high temperature, and tedious synthetic procedures should be suitable for large-scale preparation of self-supporting catalysts. As a proof of concept, we prepared electrodes with sizes of 20 cm × 15 cm (Fig. 2). After Ru^{3+} reacted with Ni, the color of the nickel

foam turned black-brown, indicating a uniform transformation by the corrosion engineering (Fig. 2(a)). In addition, the microstructure of this large-area electrode is extremely consistent, as shown by the area-selective (Areas i, ii, and iii) SEM images (Fig. 2(a)). This well-defined morphological consistency proves an identical microstructure of the large-area electrode. Likewise, the conclusion holds true for the 20 cm × 15 cm sized W-NiFe electrodes (Fig. 2(b)).

This high reproducibility was further confirmed by the electrochemical measurement. To accurately describe and evaluate the uniformity of catalytic performance of a large-area electrode, we divided the large-area electrode into 100 small samples and randomly selected 32 samples for testing (referred to as S1–S32). As shown in Fig. S11(a) in the ESM, the LSV curves for the selected samples (S1–S32) from the large-area V-RuNi electrode essentially overlap, indicating a high degree of uniformity in their catalytic performance. Furthermore, in the polar histogram of Fig. 2(c), these samples demonstrate nearly identical overpotentials at a range of current densities (10, 50, 100 mA·cm^{-2}), which underscores the consistent and reproducible HER catalytic activity of V-RuNi large-area electrode. Similarly, these selected samples from large-area W-NiFe electrodes also exhibit coincident LSV curves (Fig. S11(b) in the ESM) and nearly identical overpotentials at various current densities (Fig. 2(d)).

To more precisely ascertain the trend of overpotential variation for the selected samples (S1–S32) across different current densities (10–200 mA·cm^{-2}), we employed an error line chart for a quantitative analysis. As shown in Fig. 2(e), the chart provides a clear and detailed representation of the overpotential changes under varying current densities. Upon an increase in current densities, there is a slight tendency for the standard deviation of the overpotential to rise. In the case of selected V-RuNi catalysts for the HER, the standard deviation of their overpotentials at a current density of 10 mA·cm^{-2} is 4.7 mV. When the current density is further elevated to 200 mA·cm^{-2}, this value slightly increases to 8.2 mV. A similar pattern is observed for the selected W-NiFe catalysts, wherein the standard deviation of overpotentials at a current density of 10 mA·cm^{-2} is 5.1 mV, and also moderately increases to 10.5 mV at a current density of 200 mA·cm^{-2}. Based on microstructure and electrochemical performance analysis, we can conclude that the corrosion engineering and ion regulation dual-strategy cannot only effectively prepare large-scale electrodes but

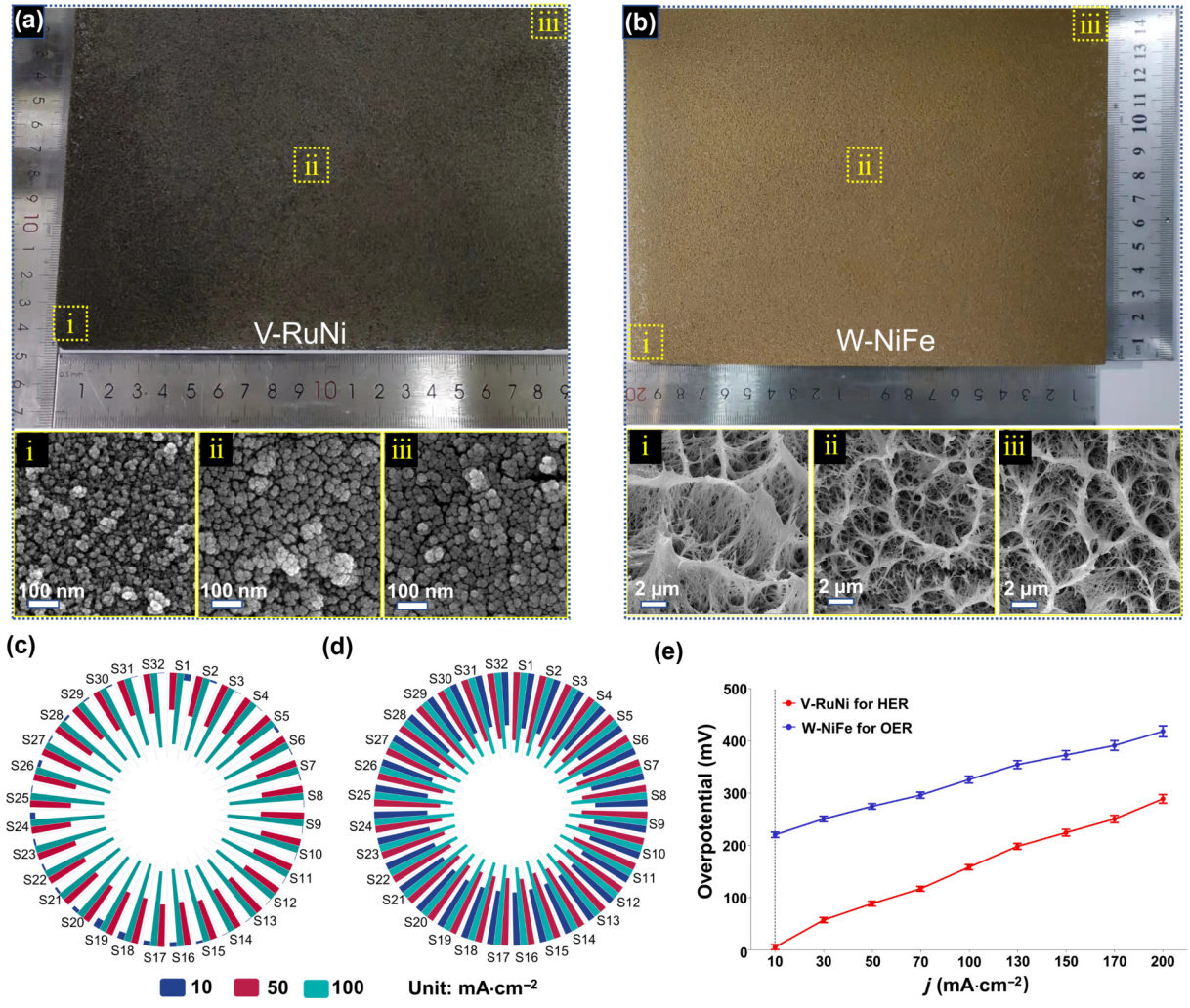

Figure 2 Size, nanostructure, and uniformity of one-step fabricated electrodes. (a) Digital photograph of V-RuNi and corresponding SEM images of three representative regions. (b) Digital photograph of W-NiFe and corresponding SEM images of three representative regions. Both electrodes are in a dimension of 20 cm × 15 cm. (c) Overpotentials of 32 V-RuNi samples (S1–S32) for HER at three current densities (10, 50, and 100 mA·cm^{-2}). (d) Overpotentials of 32 W-NiFe samples (S1–S32) for OER at three current densities (10, 50, and 100 mA·cm^{-2}). (e) Overpotential error line chart of the 32 selected samples (S1–S32) for HER and OER at various current densities.

also have excellent consistency of electrode microstructures and catalytic activities.

The catalytic properties of various electrocatalysts were evaluated in a standard three-electrode system. As shown in Fig. 3(a), during the HER process, the overpotential of V-RuNi at 100 mA·cm^{-2} is 75 mV. Interestingly, the activity of V-RuNi at high current densities is much better than that of 40% Pt/C, which might be attributed to the well-defined nanostructure of V-RuNi that can accelerate the reaction kinetics at high current densities. During the OER process, the W-NiFe exhibits the best catalytic activity among various catalysts with an overpotential of only 276 mV at 100 mA·cm^{-2}. Both V-RuNi and W-NiFe electrodes exhibit the lowest Tafel slopes of around 40 mV·dec^{-1} among all control samples (Fig. 3(b)), indicating that they can reach the desired current density at lower overpotentials. Notably, even at a large current of 500 mA·cm^{-2} (Fig. 3(c) and Fig. S12(a) in the ESM), the potential decay rate of V-RuNi is only 3.58 mV·h^{-1}, which is much lower than that of 40% Pt/C (22.6 mV·h^{-1}). The W-NiFe also achieves a small potential decay rate of 1.56 mV·h^{-1} during the OER process (Fig. 3(c) and Fig. S12(b) in the ESM), which is much smaller than that of state-of-the-art IrO_2 (6.1 mV·h^{-1}). The long-term stability of V-RuNi and W-NiFe at large current densities can be attributed to two reasons: (i) The *in-situ* growth of the active substance on the conductive substrate can reduce the interfacial impedance and enhance the charge transfer and (ii) the self-supporting structure can effectively prevent the active substance from detaching from the current collector. In addition, the dense nanoparticle morphology and microporous nanowire array structure are conducive to bubble gas release at high current densities [33, 34]. When compared to the previously reported catalysts, the overpotentials and Tafel slopes of our synthesized catalysts (V-RuNi and W-NiFe) show certain advantages (Fig. 3(d) and Tables S1 and S2 in the ESM).

Systematic measurement and analysis were employed to better elucidate the modulation of physicochemical properties brought by V/W ion regulation. The electrochemically active surface area

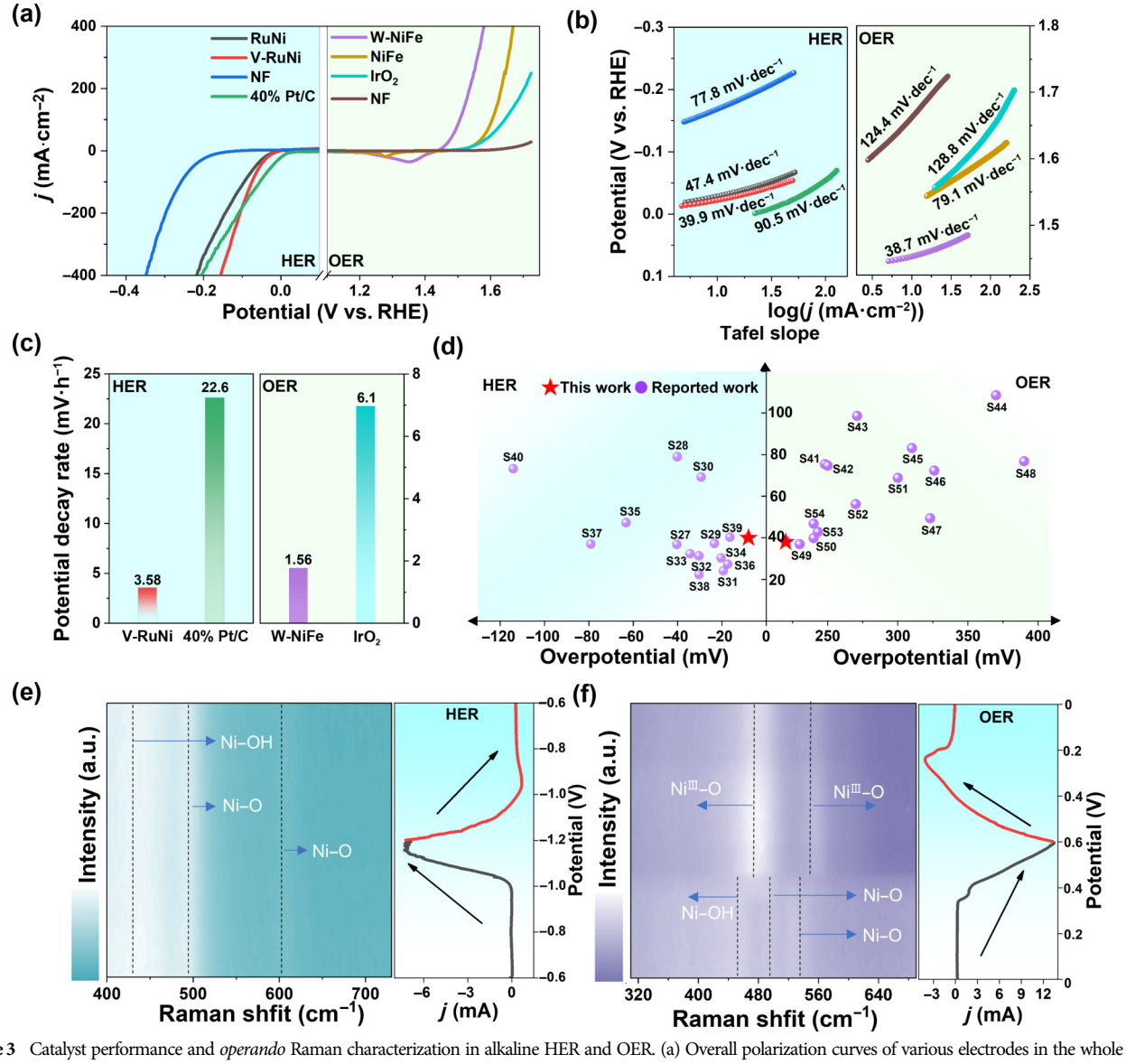

Figure 3 Catalyst performance and *operando* Raman characterization in alkaline HER and OER. (a) Overall polarization curves of various electrodes in the whole HER and OER region. (b) The corresponding Tafel plots. (c) Comparison of the potential decay rate of various electrocatalysts at the current of 500 mA·cm^{-2}. (d) Activity (η@10 mA·cm^{-2}, where η represents overpotential) and Tafel slope comparison between V-RuNi, W-NiFe, and other reported electrocatalysts (data are in Tables S1 and S2 in the ESM). *Operando* Raman spectra of (e) V-RuNi and (f) W-NiFe during the initial CV cycle.

(ECSA) of various electrocatalysts was assessed by electrochemical double-layer capacitance (C_{dl}) measurements. As shown in Figs. S13 and S14 in the ESM, the ion-induced electrocatalysts (V-RuNi and W-NiFe) achieve higher active surface areas than their RuNi/NiFe counterparts. Furthermore, the electrochemical impedance spectroscopy measurement manifests smaller charge transfer resistance of V-RuNi and W-NiFe (Fig. S15 in the ESM), indicating faster electron transfer processes [35]. During the HER and OER process, H_2 and O_2 bubble release behaviors at gas–solid–liquid (l) three-phase interfaces influence the reaction kinetics and the interaction of the active site with the reactants [36]. As displayed in Figs. S16 and S17 in the ESM, the H_2 and O_2 bubbles are pinned on the surface of the bare NF, whereas they detach very rapidly from the surface of V-RuNi and W-NiFe without retention. This interesting phenomenon illustrates that the nanostructures (nanoparticles and nanowire arrays) constructed by the V/W ion regulation strategy can reduce interfacial adhesion of bubbles, and this superaerophobic property can accelerate the release of generated bubbles and the re-exposure of the active sites to the reactant, thus promoting the reaction kinetics [37]. During the catalytic reaction, in terms of optical microscopy, it is also observed that numerous bubbles accumulate on the surfaces of Pt/C and IrO_2 electrodes and cannot be released rapidly (Fig. S18 in the ESM). In contrast, under the same test conditions, there is no noticeable bubble accumulation on the surface of V-RuNi and W-NiFe.

The possible surface reconstruction, phase evolution, and valence state changes of V-RuNi and W-NiFe during the catalytic process were investigated. First, the *operando* Raman spectroscopy was employed to probe the phase evolution during the real-time catalytic process, and the cyclic voltammetry (CV) measurements were used to provide the applied voltage under actual HER (−1.2–−0.6 V vs. Ag/AgCl) and OER (0–0.6 V vs. Ag/AgCl) conditions. During the HER process with varying voltage, there is no new characteristic peak in the *operando* Raman spectra of V-RuNi (Fig. 3(e) and Fig. S19(a) in the ESM), and the spectra always maintain the initial state. In the *ex-situ* XPS spectra (Fig. S20 in the ESM), the valence state and binding energy of Ni species do not change after the HER process, and the valence states of the Ru species are still Ru^{4+} and Ru^0. Hence, the V-RuNi has no phase evolution and surface reconstruction in the HER process. As for W-NiFe, notably, the phase evolution can be clearly detected in the *operando* Raman spectra. As shown in Fig. 3(f) and Fig. S19(b) in the ESM, when the applied voltage varies from 0 to 0.34 V vs. Ag/AgCl, two characteristic peaks at 450 and 529 cm^{-1} emerge, which are attributed to the A_{1g} stretching modes of Ni^{II}–OH and Ni^{II}–O for $Ni(OH)_2$, respectively [38, 39]. The prominent peak emerges at around 490 cm^{-1}, which is ascribed to the E_g bending vibration of Ni^{III}–O. When the applied voltage increases from the onset potential (0.34 V) to 0.6 V and during the reverse stage (0.6–0 V), the characteristic peak of $Ni(OH)_2$ disappears, and two new peaks appear at 479 and 560 cm^{-1}, owing to the E_g bending vibration and the A_{1g} stretching vibration of Ni^{III}–O in NiOOH, respectively [40]. This result demonstrates that the surface species of W-NiFe transforms from $Ni(OH)_2$ to NiOOH during the OER process, and this transformation is irreversible. In the high-resolution Ni 2p XPS spectra (Fig. S21(a) in the ESM), the valence state of Ni partially changes from the initial Ni^{2+} to Ni^{3+}, which is consistent with the *operando* Raman results. The state of Fe maintains Fe^{3+} after the OER process (Fig. S21(b) in the ESM). In short, V-RuNi exists stably during the HER process, while the W-NiFe undergoes surface reconstruction during the OER process.

First-principles calculations were carried out to unveil the doping effect on the enhanced electrocatalytic water splitting activity of the Ni-based electrode. The NiOOH (001) and NiO (001) surfaces are regarded as dominant atomic configurations at anodic (OER) and cathodic (HER) Ni-based electrodes during water splitting, respectively [41, 42]. The atomic structures of pure, Fe-doped, and Fe and W co-doped NiOOH (001), and those of pure, Ru-doped, and Ru and V co-doped NiO (001) are built according to the experiments, as shown in Figs. S22 and S23 in the ESM. The most stable doped surfaces at given doping ratios are applied for further studies, e.g., $Fe_{1/6}Ni_{5/6}OOH$, $W_{1/18}Fe_{3/18}Ni_{14/18}OOH$, $Ru_{1/4}Ni_{3/4}O$, and $V_{1/32}Ru_{8/32}Ni_{23/32}O$. The calculated free energy changes of OER steps (Fig. 4(a)) on NiOOH, $Fe_{1/6}Ni_{5/6}OOH$, and $W_{1/18}Fe_{3/18}Ni_{14/18}OOH$ are displayed in Fig. 4(b), and the potential-determine step (PDS) for the three surfaces is identified to be *OOH formation step ($H_2O(l) + *O \rightarrow *OOH + H^+ + e^-$). The atomic structures of OER intermediates are given in Fig. S24 in the ESM. The free energy change for PDS (OER overpotential) are determined to be 1.98 eV (0.75 eV), 1.90 eV (0.67 eV), and 1.58 eV (0.35 eV) on NiOOH, $Fe_{1/6}Ni_{5/6}OOH$, and $W_{1/18}Fe_{3/18}Ni_{14/18}OOH$, respectively. The decreased trend of overpotential values (0.75 eV → 0.67 eV → 0.35 eV) indicates that Fe-doping could increase the OER activity of NiOOH, and W co-doping will further increase the OER activity of Fe-doped NiOOH. The above calculated results show the synergistic effect of doped W and Fe on enhancing the OER activity of NiOOH. In addition, the calculated OER overpotential on NiOOH (001) is close to previous work, verifying the reliability of our results [43]. Besides, the HER activities on pristine, Ru-doped, and Ru and V co-doped NiO are also examined by hydrogen adsorption ability (ΔG_H). Figure 4(d) displays the mechanism of HER, and the possible H adsorption sites are given in Fig. S25 in the ESM. Figure 4(e) shows that calculated ΔG_H on NiO, $Ru_{1/4}Ni_{3/4}O$, and $V_{1/32}Ru_{8/32}Ni_{23/32}O$ are 1.45, −0.11, and −0.08 eV, respectively. The closer to zero of the ΔG_H, the higher HER activity of the corresponding surface. Accordingly, the surface in order of increasing HER activity will be NiO ($|\Delta G_H|$ = 1.45 eV), $Ru_{1/4}Ni_{3/4}O$ ($|\Delta G_H|$ = 0.11 eV), and $V_{1/32}Ru_{8/32}Ni_{23/32}O$ ($|\Delta G_H|$ = 0.08 eV). Similar to the OER analysis, the synergistic effect of doped Ru and V is also important in enhancing the HER activity of NiO.

The electronic structures, including density of states (DOS) and band center, are applied to explain the enhanced OER activity on NiOOH and HER activity on NiO by doping, as shown in Figs. 4(c) and 4(f). According to band center theory, the closer to the Fermi level of the band center, the stronger the adsorption ability the catalytic site owns. As the third OER step ($H_2O(l) + *O \rightarrow *OOH + H^+ + e^-$) is PDS on NiOOH and its corresponding doped surfaces, the free energy change of PDS (OER overpotential) could be regarded as the addition of OH adsorption ability (ΔG_{OH_*O}) at intermediate O site and one constant value [44]. According to band center theory, the increasing trend of negative intermediate O p-band center values on NiOOH (−2.17 eV), $Fe_{1/6}Ni_{5/6}OOH$ (−2.08 eV), and $W_{1/18}Fe_{3/18}Ni_{14/18}OOH$ (−1.93 eV) will lead to an increasing trend of OH adsorption ability at intermediate O, which in turn leads to the decreasing trend of overpotential on the three surfaces. Thus, the increased p-band center of intermediate O tuned by local dopants (Fe and W) is the main factor of increased OER activity on Fe and W co-doped NiOOH. In the case of HER, the d-band center values are greatly affected by element types. In detail,

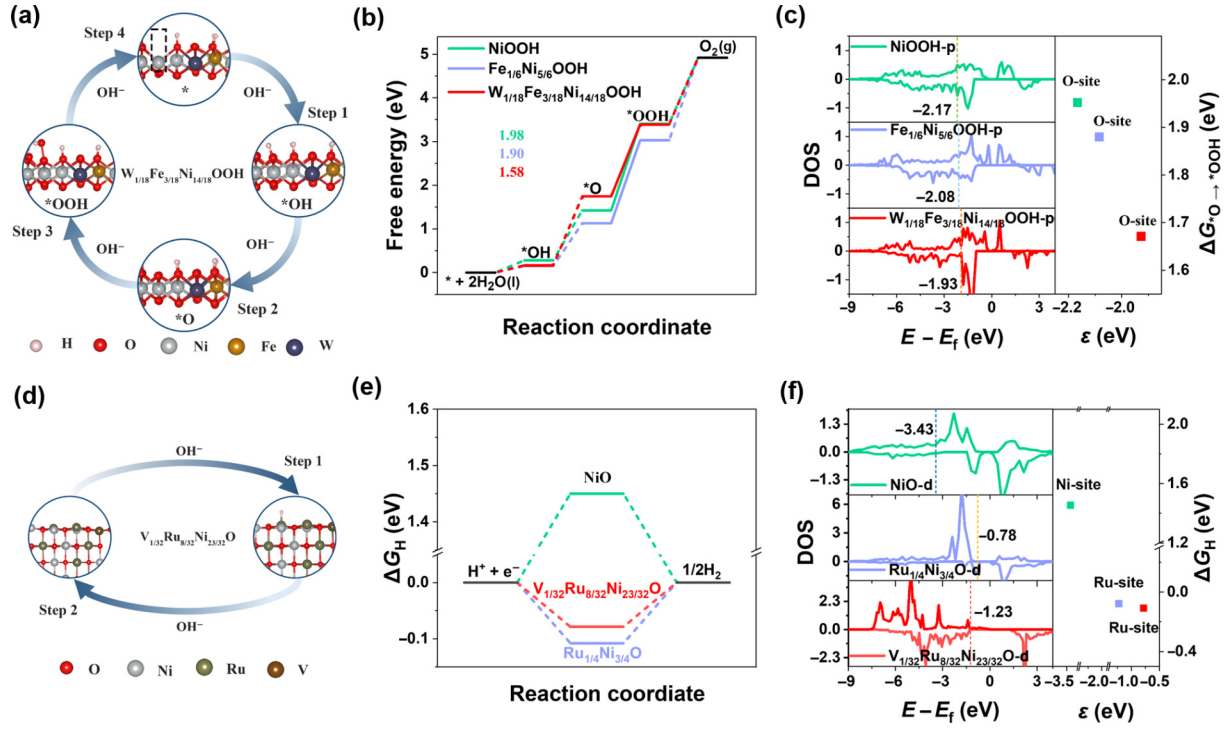

Figure 4 Theoretical insights into OER and HER mechanism. (a) Schematic diagram of the proposed OER mechanism. (b) The free energy diagram of OER. The PDS is marked by solid lines. (c) DOS and relationship between p-band center and free energy change of PDS. (d) Schematic diagram of proposed HER mechanism. (e) The free energy diagram of HER. (f) DOS and relationship between d-band center and ΔG_H on NiO, $Ru_{1/4}Ni_{3/4}O$, and $V_{1/32}Ru_{8/32}Ni_{23/32}O$.

Ru d-band centers of $Ru_{1/4}Ni_{3/4}O$ (−1.23 eV), and $V_{1/32}Ru_{8/32}Ni_{23/32}O$ (−0.78 eV) are less negative than Ni d-band center (−3.43 eV) of NiO, leading to the stronger hydrogen adsorption abilities (−0.11 and −0.08 eV) of Ru in former two surfaces than that of Ni in NiO (1.45 eV). The further doped V in $Ru_{1/4}Ni_{3/4}O$ make the Ru d-band center increase from −1.23 to −0.78 eV, leading to less negative ΔG_H (−0.11 → −0.08 eV) and highest HER activity of $V_{1/32}Ru_{8/32}Ni_{23/32}O$. These theoretical calculations also agree with experiments, confirming that the doping of V and W can effectively modulate the electronic structure, thereby improving the catalytic activity of Ni-based electrodes.

Encouraged by the outstanding catalytic performances of V-RuNi and W-NiFe for the HER and OER, respectively, we fabricated an AEM water electrolyzer (AEM-WE) to drive overall water splitting (Fig. 5(a)). For comparison, the state-of-the-art 40% Pt/C paired with IrO_2 was also used in an electrolyzer (denoted as Pt/C//IrO_2). As shown in Fig. 5(b), the cell voltage of V-RuNi//W-NiFe is 2.51 V at a high current of 1 A·cm^{-2} at 25 °C, much lower than Pt/C//IrO_2 (2.81 V) under the same conditions. When the current density is 1 A·cm^{-2}, the cell voltages of V-RuNi//W-NiFe are smaller than that of Pt/C//IrO_2 at various temperatures (Fig. 5(c) and Fig. S26 in the ESM), indicating that V-RuNi//W-NiFe-based AEM-WE cells have lower input power in industrialized water electrolysis systems. The V-RuNi//W-NiFe shows a smaller charge-transfer resistance (R_{ct}) than that of Pt/C//IrO_2 (Fig. 5(d)), which suggests the high charge transfer efficiency in these nano-ordered self-supporting electrodes. In addition, for industrial applications, the stability of the catalyst at large currents is an important parameter, so we measured the long-term stability of the V-RuNi//W-NiFe at 500 mA·cm^{-2}. As shown in Fig. 5(e), after 390 h of the galvanostatic test, the cell voltage of V-RuNi//W-NiFe shows a negligible change in the required potential. Our V-RuNi//W-NiFe-based AEM-WE cell is more durable than the recently reported catalysts for AEM-WE at 500 mA·cm^{-2} (Fig. S27 in the ESM).

To check the possible composition and phase evolution of V-RuNi and W-NiFe, post-mortem analyses are conducted using XPS, Raman, and TEM-energy dispersive X-ray spectroscopy (EDS) measurements after 100 h AEM-WE test at 500 mA·cm^{-2}. It is found that Ru and Ni in the V-RuNi catalyst are present in the oxidation states of Ru^{4+} and Ni^{2+}, respectively. The catalyst retains its hydroxide phase and nanoparticle structure with uniform distribution of V element (Fig. S28 in the ESM). However, the phase and nanostructure of W-NiFe are changed (Fig. S29 in the ESM), which underwent a phase transition from hydroxide to oxyhydroxide [45, 46]. Ultra-thin nanosheets are present on the surface of the W-NiFe nanowires, which is likely caused by surface reconstruction to generate Ni_xFe_yOOH [36, 47]. The *operando* Raman spectroscopy and post-mortem analyses jointly confirm that W-NiFe undergoes irreversible surface reconstruction to produce Ni_xFe_yOOH during the OER process. At a constant current of 500 mA·cm^{-2}, the amount of H_2 and O_2 gas produced increases linearly with a molar ratio of approximately 2 (inset of Fig. 5(e)). The yield ratio is consistently maintained at 2 within more than 100 h test and the Faraday efficiencies are nearly 100%.

To illustrate the scale-up production capability of V-RuNi and W-NiFe catalysts, a larger AEM-WE with electrode area of 19 cm × 19 cm was assembled. The large-area AEM-WE shows a nearly linear increase in cell voltage with increasing currents up to 20 A (Fig. 5(f)). In addition, the V-RuNi//W-NiFe electrolyzer exhibits significantly better activity than the Pt/C//IrO_2 electrolytic cell. When operating at a constant current of 10 A, the cell continuously operates for up to 200 h (Fig. 5(g)). Hence, our V-RuNi and W-NiFe electrodes have the potential for industrial-scale water electrolysis.

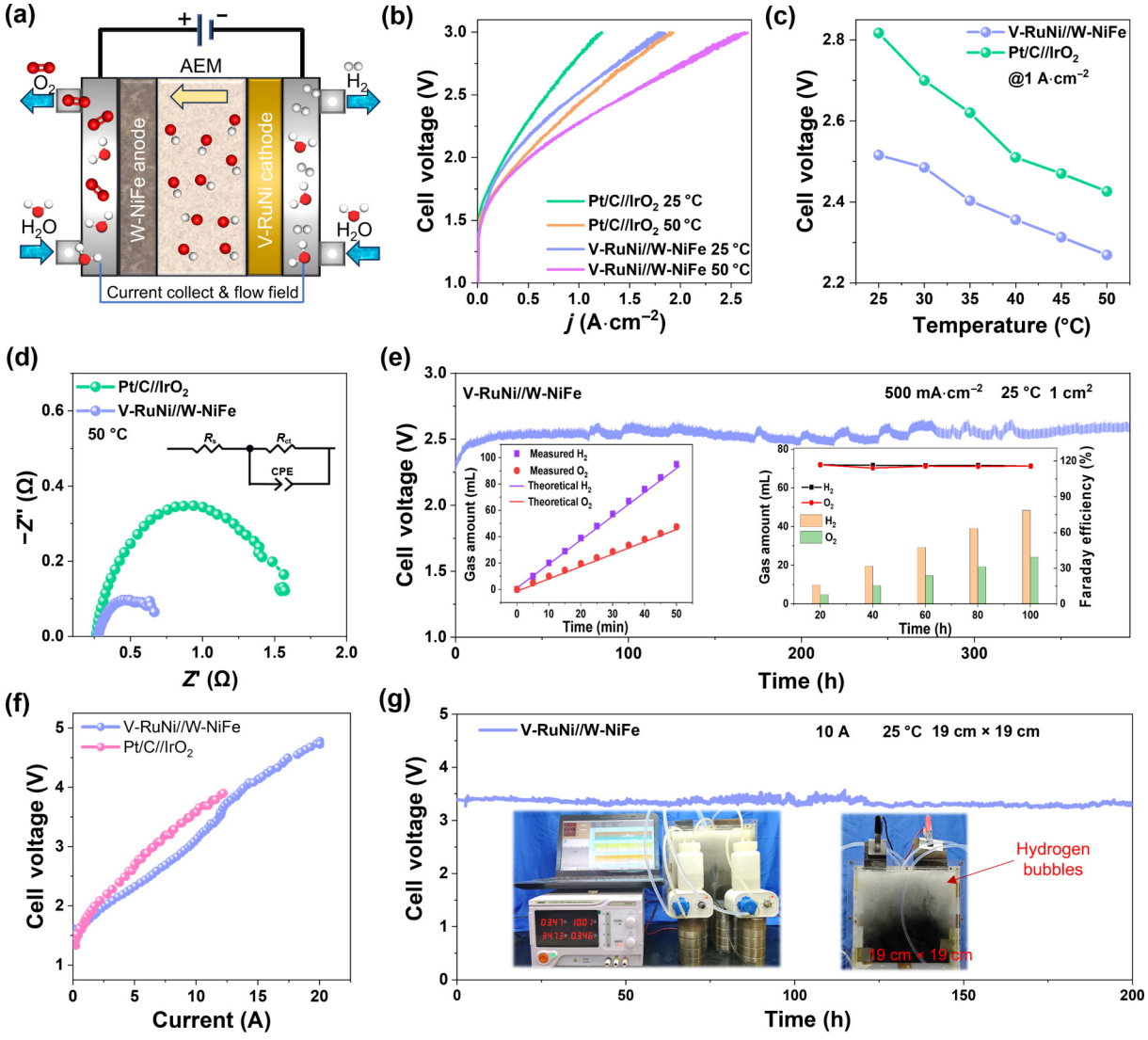

Figure 5 Performance of AEM water electrolyzer. (a) Schematic of the AEM-WE cell configuration. (b) Polarization curves of the Pt/C//IrO_2 and V-RuNi//W-NiFe at 25 and 50 °C in 1 M KOH without *iR* correction. (c) The AEM-WE cell voltages at 1 A·cm^{-2} under various temperatures. (d) Nyquist impedance plots at 50 °C in 1 M KOH. (e) Chronopotentiometric curve of V-RuNi//W-NiFe at 500 mA·cm^{-2}. Insets are the Faraday efficiency and measured gaseous amounts from the V-RuNi//W-NiFe at a current density of 500 mA·cm^{-2} in 1 M KOH. (f) Polarization curves of the V-RuNi//W-NiFe and Pt/C//IrO_2 for large area electrolyzer (19 cm × 19 cm) at 25 °C in 1 M KOH without *iR* correction. (g) Chronopotentiometric curve of V-RuNi//W-NiFe for large area electrolyzer at 10 A.

3 Conclusions

We have achieved efficient HER and OER electrocatalysts through an energy- and time-efficient strategy based on corrosion engineering and ion regulation. This synthesis strategy is scalable and can generate highly uniform surface nanostructure and stable catalytic activity. As a case study, the as-prepared electrodes (V-RuNi and W-NiFe) possess well-designed nanoarray architectures, superaerophobic surface, and a robust interface with the Ni backbone. The associated large active surface areas and fast reaction kinetics endow the V-RuNi and W-NiFe electrodes with stable catalytic activity toward HER (overpotential is 75 mV at 100 mA·cm^{-2}) and OER (overpotential is 276 mV at 100 mA·cm^{-2}), respectively. Theoretical simulation shows that the increased p-band center of the intermediate oxygen species, modulated by local dopants (Fe and W), enhances the adsorption affinity for OH at the intermediate oxygen site. This effect, in turn, lowers the free energy associated with the *OOH formation step, thereby augmenting the OER activity. In addition, the synergistic doping of Ru and V reduces the ΔG_H value of cathodic catalyst, thereby boosting the HER activity. The large-area AEM-WE exhibits a nearly linear increase in cell voltage with increasing currents up to 20 A and stable operation for up to 200 h at a constant current of 10 A.

Given that the electrodes are fabricated from inexpensive raw materials in a facile way and are scalable (the size in this study, 19 cm × 19 cm, is limited only by the synthesis apparatus), our synthetic method for HER and OER catalysts has the potential to bridge the gap between fundamental science and industrial water splitting.

Electronic Supplementary Material: Supplementary material (including catalyst preparation methods and electrochemical measurements; calculation procedures; XRD, SEM, TEM, Raman spectroscopy; thermogravimetric analyses; electrochemical data; computational models; and tables) is available in the online version of this article at https://doi.org/10.26599/NR.2026.94908557.

Data availability

All data needed to support the conclusions in the paper are presented in the manuscript and the Electronic Supplementary Material. Additional data related to this paper may be requested from the corresponding author upon request.

Acknowledgements

This work was financially supported by the 10th Young Elite Scientists Sponsorship Program by CAST, the National Key Research and Development Program of China (No. 2023YFB3809700), the Ministry of Education (No. 8091B03052402), Guangzhou Basic and Applied Basic Research Foundation (Nos. 2024A04J3771 and 2024A04J3154), and the National Natural Science Foundation of China (Nos. 52172202 and 12174154).

Declaration of competing interest

All the contributing authors report no conflict of interests in this work.

Author contribution statement

H. L.: Investigation, original draft writing, data analysis. Y. F. Z. and Q. X. W.: Investigation, electrochemical performance testing and analysis. M.-Q. C. and X.-B. L.: Theoretical simulation. X. L. Y. and W. J. M.: Review, supervision. Z. L. W. and S. C. M.: Conceptualization, review, supervision. All the contributing authors report no conflict of interests in this work.

Use of AI statement

None.

References

[1] Pei, Z. X.; Tan, H.; Gu, J. X.; Lu, L. G.; Zeng, X.; Zhang, T. Q.; Wang, C.; Ding, L. Y.; Cullen, P. J.; Chen, Z. F. et al. A polymeric hydrogel electrocatalyst for direct water oxidation. *Nat. Commun.* **2023**, *14*, 818.

[2] Zheng, C. Y.; Zhang, X.; Zhou, Z.; Hu, Z. P. A first-principles study on the electrochemical reaction activity of 3D transition metal single-atom catalysts in nitrogen-doped graphene: Trends and hints. *eScience* **2022**, *2*, 219–226.

[3] Wen, Y. Z.; Liu, C.; Huang, R.; Zhang, H.; Li, X. B.; García de Arquer, F. P.; Liu, Z.; Li, Y. Y.; Zhang, B. Introducing Brønsted acid sites to accelerate the bridging-oxygen-assisted deprotonation in acidic water oxidation. *Nat. Commun.* **2022**, *13*, 4871.

[4] Du, J. L.; Xiang, D. L.; Zhou, K. X.; Wang, L. C.; Yu, J. Y.; Xia, H. H.; Zhao, L. L.; Liu, H.; Zhou, W. J. Electrochemical hydrogen production coupled with oxygen evolution, organic synthesis, and waste reforming. *Nano Energy* **2022**, *104*, 107875.

[5] Haase, F. T.; Bergmann, A.; Jones, T. E.; Timoshenko, J.; Herzog, A.; Jeon, H. S.; Rettenmaier, C.; Cuenya, B. R. Size effects and active state formation of cobalt oxide nanoparticles during the oxygen evolution reaction. *Nat. Energy* **2022**, *7*, 765–773.

[6] Tang, L.; Xia, M. H.; Cao, S. Y.; Bo, X.; Zhang, S. B.; Zhang, Y. L.; Liu, X.; Zhang, L. Z.; Yu, L.; Deng, D. H. *Operando* identification of active sites in Co–Cr oxyhydroxide oxygen evolution electrocatalysts. *Nano Energy* **2022**, *101*, 107562.

[7] Zeng, F.; Mebrahtu, C.; Liao, L. F.; Beine, A. K.; Palkovits, R. Stability and deactivation of OER electrocatalysts: A review. *J. Energy Chem.* **2022**, *69*, 301–329.

[8] Li, Y. T.; Dai, T. Y.; Wu, Q. X.; Lang, X. Y.; Zhao, L. J.; Jiang, Q. Design heterostructure of NiS–NiS_2 on NiFe layered double hydroxide with Mo doping for efficient overall water splitting. *Mater. Today Energy* **2022**, *23*, 100906.

[9] Adiga, P.; Nunn, W.; Wong, C.; Manjeshwar, A. K.; Nair, S.; Jalan, B.; Stoerzinger, K. A. Breaking OER and CER scaling relations via strain and its relaxation in RuO_2 (101). *Mater. Today Energy* **2022**, *28*, 101087.

[10] Zhang, X. Y.; Li, Y. X.; Wu, Z. J.; Sheng, H. B.; Hu, Y. B.; Li, C.; Li, H. Y.; Cao, L. X.; Dong, B. H. Crystalline/amorphous composite interface induced by $NaBH_4$ hydrolysis reaction: A new interfacial electrocatalyst for efficient oxygen evolution reaction. *Mater. Today Energy* **2022**, *26*, 100987.

[11] Lei, H.; Wan, Q. X.; Tan, S. Z.; Wang, Z. L.; Mai, W. J. Pt-quantum-dot-modified sulfur-doped NiFe layered double hydroxide for high-current-density alkaline water splitting at industrial temperature. *Adv. Mater.* **2023**, *35*, 2208209.

[12] Lei, H.; Ma, L.; Wan, Q. X.; Huangfu, Z. W.; Tan, S. Z.; Wang, Z. L.; Mai, W. Porous carbon nanofibers confined NiFe alloy nanoparticles as efficient bifunctional electrocatalysts for Zn–air batteries. *Nano Energy* **2022**, *104*, 107941.

[13] Zhang, T.; Liu, Y. P.; Ye, Q. T.; Fan, H. J. Alkaline seawater electrolysis at industrial level: Recent progress and perspective. *J. Electrochem.* **2022**, *28*, 2214006.

[14] Chen, H.; Li, J. H.; Shen, Y. C.; Jiao, W. Q.; Wang, J. P.; Zou, Y. C.; Zou, X. X. Room temperature, fast fabrication of square meter-sized oxygen evolution electrode toward industrial alkaline electrolyzer. *Appl. Catal. B: Environ.* **2022**, *316*, 121605.

[15] Cheng, Y. K.; Fu, P. J.; Yu, Z. P.; Yang, X. D.; Zhang, Y. R.; Yuan, A. J.; Liu, H.; Du, J. H.; Chen, L. Modulation of the multiphase phosphorus/sulfide heterogeneous interface via rare earth for solar-enhanced water splitting at industrial-level current densities. *Carbon Neutralization* **2024**, *3*, 873–887.

[16] Zhou, W. B.; Huang, Y. C.; Cai, H. Q.; Wang, T.; Li, H. T.; Zhang, C.; Zhao, L. M.; Chen, L. L.; Liao, M. H.; Tang, Z. Q. et al. A strongly coupled cluster heterostructure with Pt–N–Mo bonding for durable and efficient H_2 evolution in anion-exchange membrane water electrolyzers. *Nano-Micro Lett.* **2025**, *17*, 296.

[17] Zhai, W. F.; Chen, Y.; Liu, Y. D.; Ma, Y. Y.; Vijayakumar, P.; Qin, Y. B.; Qu, Y. Q.; Dai, Z. F. Covalently bonded Ni sites in black phosphorene with electron redistribution for efficient metal-lightweighted water electrolysis. *Nano-Micro Lett.* **2024**, *16*, 115.

[18] Sun, F.; Qin, J. S.; Wang, Z. Y.; Yu, M. Z.; Wu, X. H.; Sun, X. M.; Qiu, J. S. Energy-saving hydrogen production by chlorine-free hybrid seawater splitting coupling hydrazine degradation. *Nat. Commun.* **2021**, *12*, 4182.

[19] Teng, X.; Si, D.; Chen, L. S.; Shi, J. L. Synergetic catalytic effects by strong metal–support interaction for efficient electrocatalysis. *eScience* **2024**, *4*, 100272.

[20] Yu, L.; Wu, L. B.; McElhenny, B.; Song, S. W.; Luo, D.; Zhang, F. H.; Yu, Y.; Chen, S.; Ren, Z. F. Ultrafast room-temperature synthesis of porous S-doped Ni/Fe(oxy) hydroxide electrodes for oxygen evolution catalysis in seawater splitting. *Energy Environ. Sci.* **2020**, *13*, 3439–3446.

[21] Liu, X. P.; Gong, M. X.; Xiao, D. D.; Deng, S. F.; Liang, J. N.; Zhao, T. H.; Lu, Y.; Shen, T.; Zhang, J.; Wang, D. L. Turning waste into treasure: Regulating the oxygen corrosion on Fe foam for efficient electrocatalysis. *Small* **2020**, *16*, 2000663.

[22] Gao, L.; Zhang, L. L.; Yang, X. L. N, S-codoped porous carbon nanosheets decorated with Fe_3C nanoparticles as high-performance anode materials for lithium ion hybrid supercapacitors. *Rare Met.* **2022**, *41*, 2517–2526.

[23] Yuan, W. Z.; Jiang, T. F.; Fang, X. Q.; Fan, Y.; Qian, S.; Gao, Y. Y.; Cheng, N. Y.; Xue, H. G.; Tian, J. Q. Interface engineering of S-doped Co_2P@Ni_2P core–shell heterostructures for efficient and energy-

saving water splitting. *Chem. Eng. J.* **2022**, *439*, 135743.
[24] Liu, X.; Wu, G.; Li, Q. Orbital modulation in platinum-group-metal (PGM) electrocatalysts: An effective approach to boost catalytic performance. *eScience* **2025**, *5*, 100270.
[25] Wu, Z. X.; Zhao, Y.; Wu, H. B.; Gao, Y. X.; Chen, Z.; Jin, W.; Wang, J. S.; Ma, T. Y.; Wang, L. Corrosion engineering on iron foam toward efficiently electrocatalytic overall water splitting powered by sustainable energy. *Adv. Funct. Mater.* **2021**, *31*, 2010437.
[26] Zhang, X. Y.; Li, F. T.; Dong, Y. W.; Dong, B.; Dai, F. N.; Liu, C. G.; Chai, Y. M. Dynamic anion regulation to construct S-doped FeOOH realizing 1000 mA·cm^{-2}-level-current-density oxygen evolution over 1000 h. *Appl. Catal. B: Environ.* **2022**, *315*, 121571.
[27] Yan, Z. H.; Sun, H. M.; Chen, X.; Liu, H. H.; Zhao, Y. R.; Li, H. X.; Xie, W.; Cheng, F. Y.; Chen, J. Anion insertion enhanced electrodeposition of robust metal hydroxide/oxide electrodes for oxygen evolution. *Nat. Commun.* **2018**, *9*, 2373.
[28] Liu, Y. P.; Liang, X.; Gu, L.; Zhang, Y.; Li, G. D.; Zou, X. X.; Chen, J. S. Corrosion engineering towards efficient oxygen evolution electrodes with stable catalytic activity for over 6000 hours. *Nat. Commun.* **2018**, *9*, 2609.
[29] Qiu, Y.; Rao, Y. F.; Zheng, Y. N.; Hu, H.; Zhang, W. H.; Guo, X. H. Activating ruthenium dioxide via compressive strain achieving efficient multifunctional electrocatalysis for Zn–air batteries and overall water splitting. *InfoMat* **2022**, *4*, e12326.
[30] Lei, H.; Yang, S. J.; Wan, Q. X.; Ma, L.; Javed, M. S.; Tan, S. Z.; Wang, Z. L.; Mai, W. Coordination and interface engineering to boost catalytic property of two-dimensional ZIFs for wearable Zn–air batteries. *J. Energy Chem.* **2022**, *68*, 78–86.
[31] Zhang, T.; Liu, Y. P.; Tong, L.; Yu, J.; Lin, S. W.; Li, Y.; Fan, H. J. Oxidation state engineering in octahedral Ni by anchored sulfate to boost intrinsic oxygen evolution activity. *ACS Nano* **2023**, *17*, 6770–6780.
[32] Liu, H. B.; Jia, Q. H.; Huang, S. Q.; Yang, L.; Wang, S. T.; Zheng, L. R.; Cao, D. P. Ultra-small Ru nanoparticles embedded on Fe–Ni(OH)$_2$ nanosheets for efficient water splitting at a large current density with long-term stability of 680 hours. *J. Mater. Chem. A* **2022**, *10*, 4817–4824.
[33] Zhai, W. F.; Ma, Y. Y.; Chen, D.; Ho, J. C.; Dai, Z. F.; Qu, Y. Q. Recent progress on the long-term stability of hydrogen evolution reaction electrocatalysts. *InfoMat* **2022**, *4*, e12357.
[34] Jiang, L. T.; Chen, X. B.; Jiang, L. B.; Luo, X.; Li, R. D.; Zhou, Q. Q.; Mu, X. Q.; Chen, L.; Li, B.; Yu, J. et al. Hydroxyl-interfacial water proton exchange strategy to hasten water reduction on ruthenium sites. *ACS Catal.* **2025**, *15*, 14380–14391.
[35] Lei, H.; Wang, Z. L.; Yang, F.; Huang, X. Q.; Liu, J. H.; Liang, Y. Y.; Xie, J. P.; Javed, M. S.; Lu, X. H.; Tan, S. Z. et al. NiFe nanoparticles embedded N-doped carbon nanotubes as high-efficient electrocatalysts for wearable solid-state Zn–air batteries. *Nano Energy* **2020**, *68*, 104293.
[36] Liang, C. W.; Zou, P. C.; Nairan, A.; Zhang, Y. Q.; Liu, J. X.; Liu, K. W.; Hu, S. Y.; Kang, F. Y.; Fan, H. J.; Yang, C. Exceptional performance of hierarchical Ni–Fe oxyhydroxide@NiFe alloy nanowire array electrocatalysts for large current density water splitting. *Energy Environ. Sci.* **2020**, *13*, 86–95.
[37] Yu, X. X.; Yu, Z. Y.; Zhang, X. L.; Zheng, Y. R.; Duan, Y.; Gao, Q.; Wu, R.; Sun, B.; Gao, M. R.; Wang, G. X. et al. "Superaerophobic" nickel phosphide nanoarray catalyst for efficient hydrogen evolution at ultrahigh current densities. *J. Am. Chem. Soc.* **2019**, *141*, 7537–7543.
[38] Lei, H.; Ma, L.; Wan, Q. X.; Tan, S. Z.; Yang, B.; Wang, Z. L.; Mai, W.; Fan, H. J. Promoting surface reconstruction of NiFe layered double hydroxide for enhanced oxygen evolution. *Adv. Energy Mater.* **2022**, *12*, 2202522.
[39] Louie, M. W.; Bell, A. T. An investigation of thin-film Ni–Fe oxide catalysts for the electrochemical evolution of oxygen. *J. Am. Chem. Soc.* **2013**, *135*, 12329–12337.
[40] Liu, M. J.; Min, K. A.; Han, B.; Lee, L. Y. S. Interfacing or doping? Role of Ce in highly promoted water oxidation of NiFe-layered double hydroxide. *Adv. Energy Mater.* **2021**, *11*, 2101281.
[41] Zhang, T.; Wu, M. Y.; Yan, D. Y.; Mao, J.; Liu, H.; Hu, W. B.; Du, X. W.; Ling, T.; Qiao, S. Z. Engineering oxygen vacancy on NiO nanorod arrays for alkaline hydrogen evolution. *Nano Energy* **2018**, *43*, 103–109.
[42] Tkalych, A. J.; Yu, K.; Carter, E. A. Structural and electronic features of β-Ni(OH)$_2$ and β-NiOOH from first principles. *J. Phys. Chem. C* **2015**, *119*, 24315–24322.
[43] Hu, Q.; Xue, Y. F.; Kang, J. X.; Scivetti, I.; Teobaldi, G.; Selloni, A.; Guo, L.; Liu, L. M. Structure and oxygen evolution activity of β-NiOOH: Where are the protons? *ACS Catal.* **2021**, *12*, 295–304.
[44] Huang, K.; Lin, C. L.; Yu, G. Q.; Du, P.; Xie, X. Y.; He, X.; Zheng, Z. C.; Sun, N.; Tang, H. L.; Li, X. B. et al. Ru/Se–RuO$_2$ composites via controlled selenization strategy for enhanced acidic oxygen evolution. *Adv. Funct. Mater.* **2023**, *33*, 2211102.
[45] Wu, Y. J.; Song, M. L.; Huang, Y. C.; Dong, C. L.; Li, Y. Y.; Lu, Y. X.; Zhou, B.; Wang, D. D.; Jia, J. F.; Wang, S. Y. et al. Promoting surface reconstruction of NiFe layered double hydroxides via intercalating $[Cr(C_2O_4)_3]^{3-}$ for enhanced oxygen evolution. *J. Energy Chem.* **2022**, *74*, 140–148.
[46] Qiu, Z.; Ma, Y.; Edvinsson, T. In *operando* Raman investigation of Fe doping influence on catalytic NiO intermediates for enhanced overall water splitting. *Nano Energy* **2019**, *66*, 104118.
[47] Wang, X.; Yu, M. H.; Feng, X. L. Electronic structure regulation of noble metal-free materials toward alkaline oxygen electrocatalysis. *eScience* **2023**, *3*, 100141.